

Constraining baryonic feedback and cosmology with weak-lensing, X-ray, and kinematic Sunyaev-Zeldovich observations

Aurel Schneider,¹★ Sambit K. Giri,¹ Stefania Amodeo,² and Alexandre Refregier³

¹*Institute for Computational Science, University of Zurich, Winterthurerstrasse 190, 8057 Zurich, Switzerland*

²*Université de Strasbourg, CNRS, Observatoire astronomique de Strasbourg, UMR 7550, F-67000 Strasbourg, France*

³*Institute for Particle Physics and Astrophysics, ETH Zurich, Wolfgang Pauli Strasse 27, 8093 Zurich, Switzerland*

Accepted XXX. Received YYY; in original form ZZZ

ABSTRACT

Modern weak-lensing observations are becoming increasingly sensitive to baryonic feedback processes which are still poorly understood. So far, this new challenge has been faced either by imposing scale-cuts in the data or by modelling baryonic effects with simple, one-parameter models. In this paper, we rely on a more general, seven-parameter prescription of baryonic feedback effects, which is primarily motivated by observations and has been shown to agree with a plethora of hydrodynamical simulations. By combining weak-lensing data from the Kilo-Degree Survey (KiDS-1000) with observations of gas around galaxy groups and clusters, we are able to constrain our baryonic model parameters and learn more about feedback and cosmology. In particular, we use galaxy cluster gas (and stellar) fractions from a combination of X-ray data as well as stacked gas profiles measured by the Atacama Cosmology Telescope (ACT) via the kinematic Sunyaev-Zeldovich (kSZ) effect to provide evidence for baryonic feedback that is stronger than predicted by most hydrodynamical simulations. In terms of the baryonic suppression of the matter power spectrum, we report a beyond-percent effect at wave-modes above $k \sim 0.1 - 0.4$ h/Mpc and a maximum suppression of 15–35 percent at $k > 5$ h/Mpc (68 percent confidence level). Regarding the cosmological clustering strength, parametrised by the combined parameter $\Sigma_8 = \sigma_8(\Omega_m/0.3)^{0.58}$, we find the known tension with the Planck satellite data to be reduced from 3.8 to 3.2 σ once baryonic effects are fully included in the analysis pipeline. The tension is further decreased to 2.8 σ when the weak-lensing data is combined with observations from X-ray and the kSZ effect. We conclude that, while baryonic feedback effects become more important in modern weak-lensing surveys, they can be excluded as the primary culprit for the observed Σ_8 -tension.

Key words: Cosmology – Weak lensing – Baryonic feedback

1 INTRODUCTION

The standard model of cosmology (Λ CDM) based on the cosmological constant (Λ) plus cold dark matter (CDM) has so far shown to be very successful in predicting cosmological observations from many different scales and redshifts. Despite this obvious success, the model remains unsatisfactory in the sense that the nature of its two main components is not truly understood. One of the main goals of current and upcoming cosmological surveys is to stress-test the Λ CDM model using different observational probes from various scales and redshifts. Any appearing discrepancy between different observations could point towards new physics and might ultimately lead to a better understanding of the dark sector.

Over the last decade, low-redshift probes of the cosmological large-scale structure have substantially improved in accuracy. As a result, a mild yet persistent tension has appeared between the measured amplitudes of matter fluctuations compared to results from the cosmic microwave background (CMB). More specifically, the combined cosmological parameter $S_8 = \sigma_8(\Omega_m/0.3)^{0.5}$ obtained by the weak-lensing surveys CFHTLenS (Heymans et al. 2013; Joudaki et al. 2017),

KiDS (Hildebrandt et al. 2017; Asgari et al. 2021), DES (Troxel et al. 2018; Amon et al. 2021), and HSC (Hikage et al. 2019) is consistently low compared to the CMB value from Planck (Aghanim et al. 2020a). The tension is only at the 2–3.5 σ level, and therefore statistically not very significant, but it appears consistently in all weak-lensing surveys. Other low-redshift observables, such as cluster counts (Ade et al. 2016; Corasaniti et al. 2021) and CMB-lensing (Aghanim et al. 2020b; Bianchini et al. 2020), show similar trends, albeit at even lower statistical significance.

One potential systematic that low-redshift probes such as weak lensing, galaxy clustering, and cluster count measurements have to deal with is baryonic feedback, i.e. gas ejection driven by energy blasts from active galactic nuclei (AGN). Baryonic feedback leads to a redistribution of gas, altering the nonlinear density field at cosmological scales (see e.g. Chisari et al. 2019, for a comprehensive review). Based on the results from hydro-dynamical simulations, a suppression of the matter power spectrum of order 10 percent at around $k \sim 1$ h/Mpc is expected (van Daalen et al. 2011; Semboloni et al. 2011). However, the exact amplitude of the effect remains unknown (Schneider et al. 2019; van Daalen et al. 2020).

Current weak lensing surveys have either followed the strategy of modelling baryonic feedback using an additional free parameter

★ E-mail: aurel.schneider@uzh.ch

(as e.g. done by KiDS and HSC) or ignoring data from small scales, where feedback effects are believed to be significant (an approach pursued by DES). Both approaches rely on knowledge of the amplitude of feedback at different cosmological scales which are taken from hydro-dynamical simulations. However, simulations include AGN feedback as a subgrid model and cannot provide predictions from first principles. The current results from weak-lensing therefore carry a certain amount of uncertainty that is difficult to quantify.

In this paper we use an alternative approach to deal with the baryonic feedback problem. Instead of relying on results from hydro-dynamical simulations, we directly constrain baryonic effects using observed gas distributions around galaxy groups and clusters. We thereby use the baryonification model (Schneider & Teyssier 2015; Schneider et al. 2019; Giri & Schneider 2021) which provides a direct connection between halo properties (such as the gas, stellar, and dark matter profiles) and the matter power spectrum (and thus the weak-lensing signal). This allows us to perform a cosmological parameter inference study including weak-lensing data together with X-ray observations from galaxy clusters as well as the kinematic Sunyaev-Zeldovich (kSZ) signal.

We argue this to be the first study to self-consistently include baryonic feedback effects into a cosmological inference analysis without relying on hydrodynamical simulations that could include hidden biases due to the implemented AGN subgrid model. On the one hand, this approach allows us to confirm the viability of previous studies regarding baryonic feedback. On the other hand, we are able to investigate if direct gas observation provide evidence for particularly strong baryonic feedback that could alleviate the S_8 -tension.

Next to the S_8 -tension, we explore the parameter constraints of the baryonification model obtained from the KiDS weak-lensing data alone and from combinations of weak lensing with X-ray observations and the kSZ effect. Furthermore, we derive the first constraints on the baryonic suppression of the matter power spectrum, which include uncertainties from both baryonic physics and cosmology. These model-independent constraints allow us to carry out a direct comparison to results from hydrodynamical simulations.

The paper is organised as follows: In Sec. 2 we summarise the baryonification model with a focus on its free parameters that will be varied during the inference analysis. Sec. 3 provides an overview of the data products for the weak-lensing, the X-ray, and the kSZ measurements. We especially show how baryonic feedback processes affect these observations. In Sec. 4 we present the results, showing in particular the effect of baryonic feedback on the S_8 tension and the matter power spectrum. Sec. 5 finally provides a conclusion of the paper as well as an outlook towards upcoming weak-lensing surveys.

2 BARYONIFICATION MODEL

The baryonification method relies on an approach to perturbatively shift simulation particles in gravity-only N -body outputs in order to mimic the presence of gas and stars. The goal of the particle shifts is to transform the original dark-matter-only profiles (ρ_{dmo}) into more realistic dark-matter-baryon profiles (ρ_{dmb})

$$\rho_{\text{dmo}} \rightarrow \rho_{\text{dmb}} = \rho_{\text{clm}} + \rho_{\text{gas}} + \rho_{\text{cga}}, \quad (1)$$

where the latter consists of a collision-less matter (ρ_{clm}), a gas (ρ_{gas}), and a central-galaxy component (ρ_{cga}). The collision-less matter profile is dominated by dark matter but also contains a stellar part from satellite galaxies. The gas and stellar profiles consist of parametrised functions that are motivated by observations (Schneider & Teyssier

2015). They are furthermore back-reacting on the collision-less profile in a process referred to as adiabatic contraction and expansion (see e.g. Teyssier et al. 2011).

We refer to Schneider et al. (2019) and Giri & Schneider (2021) for a detailed description of the baryonification model. Here we only show some key quantities such as the gas profile

$$\rho_{\text{gas}}(r) \propto \frac{(\Omega_b/\Omega_m) - f_{\text{star}}(M_{\text{vir}})}{\left[1 + 10 \left(\frac{r}{r_{\text{vir}}}\right)\right]^{\beta(M_{\text{vir}})} \left[1 + \left(\frac{r}{\theta_{\text{ej}} r_{\text{vir}}}\right)\right]^{[\delta - \beta(M_{\text{vir}})]/\gamma}} \quad (2)$$

with mass-dependent slope

$$\beta(M_{\text{vir}}) = \frac{3(M_{\text{vir}}/M_c)^\mu}{1 + (M_{\text{vir}}/M_c)^\mu}, \quad (3)$$

where r_{vir} and M_{vir} are the virial radius and mass, respectively. Eq. (2) describes a cored power-law with a steep truncation beyond $r_{\text{ej}} = \theta_{\text{ej}} r_{\text{vir}}$. For the largest clusters ($M_{\text{vir}} \gg M_c$), the slope of the power-law approaches $\beta = 3$, which means that the profile follows a (truncated) NFW profile. This is not the case for smaller clusters and galaxy groups, where the slope becomes significantly shallower ($\beta < 3$), mimicking the effects of baryonic feedback processes.

The stellar-to-halo fractions of the central galaxy (f_{cga}) and the total stellar content (f_{star}) are given by

$$f_i(M_{\text{vir}}) = \frac{M_i}{M_{\text{vir}}} = 0.055 \left(\frac{M_s}{M_{\text{vir}}}\right)^{\eta_i} \quad (4)$$

with $i = \{\text{cga}, \text{star}\}$. Here we assume $M_s = 2 \times 10^{11} M_\odot/h$ as well as $\eta_{\text{star}} \equiv \eta$ and $\eta_{\text{cga}} \equiv \eta + \eta_\delta$. Note that Eq. (4) is motivated by the large-scale behaviour of the fitting function from Moster et al. (2013).

The baryonification model summarised above comes with seven free model parameters, five describing the gas distribution (M_c , μ , θ_{ej} , γ , δ) and two the stellar abundances (η , η_δ). Although it is shown in Giri & Schneider (2021) that three parameters are sufficient to recover the results from known hydrodynamical simulations, we will simultaneously vary all seven parameters in this paper. This is a very conservative choice motivated by the fact that we do not know if current simulations properly model the gas distribution at cosmological scales.

One of the main advantages of the baryonification model is that it connects the distribution of gas and stars around haloes with statistics of the large-scale structure, such as the matter power spectrum. This allows us to not only quantify the effects of baryonic feedback on weak-lensing statistics, but to connect weak-lensing results with observations of gas around galaxy groups and clusters. We will thereby focus on observations from X-ray gas fractions and gas profiles measured by the kSZ effect.

Note that for this paper, whenever we require information about the matter power spectrum, we will use the baryonic emulator of Giri & Schneider (2021) instead of directly applying the baryonification model to N -body simulations. The baryonic emulator has been built using 2700 baryonified simulation outputs, randomly distributed over the full parameter space. It provides percent accurate predictions of the baryonic power suppression signal and is fast enough to be readily used for a multi-parameter Bayesian analysis.

3 DATA AND ANALYSIS PIPELINE

In this section we discuss all data products used for the analysis. This includes the weak-lensing shear spectra, the X-ray cluster fractions, and the stacked gas profiles from the kSZ observations. Next to the

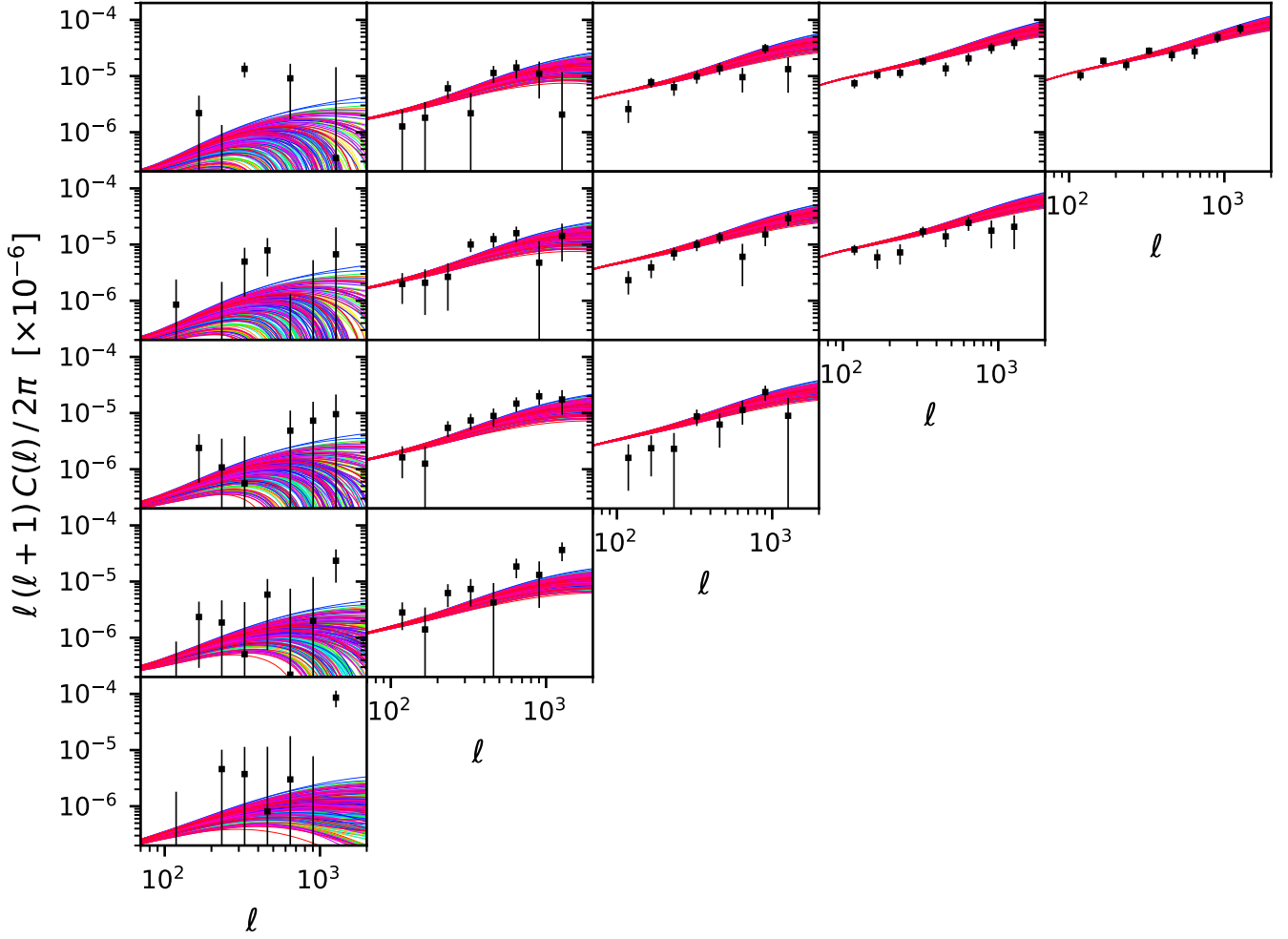


Figure 1. Angular weak-lensing shear power spectra assuming a Planck 2018 cosmology and randomly selected parameter values for the baryonification model (coloured lines). The baryonic parameters all lie within the prior range of the baryonic emulator (Giri & Schneider 2021) which provides a very conservative estimate for the current range of uncertainty due to baryonic feedback. The data points correspond to the band power from the KiDS-1000 data release (Asgari et al. 2021). Different panels show the auto- and cross-correlation spectra of the 5 different tomographic bins between $z = 0$ (bottom) and 1.5 (top).

data, we also present the analysis pipeline to predict the theory signal corresponding to each observable.

3.1 Weak-lensing shear power spectrum

For the weak-lensing shear power spectrum, we use observations from the Kilo-Degree Survey (KiDS) 1000 data release (Kuijken et al. 2019). The data contains the band power spectrum separated into 8 logarithmically spaced data points in the range $\ell \sim 100 - 2000$ and split up in five tomographic bins between $z = 0 - 1.5$ (Asgari et al. 2021). The full data vector is shown as black symbols in Fig. 1. The corresponding covariance matrix is published in Joachimi et al. (2021). The square-root of its diagonal values are shown as error-bars on the data points of Fig. 1.

The relation between the band power (C_{ij}^l) and the angular power spectrum (C_{ij}) is given by

$$C_{ij}^l = \frac{1}{2N_l} \int_0^\infty d\ell \ell W_l(\ell) C_{ij}(\ell), \quad (5)$$

where $W_l(\ell)$ are window functions for the different data-bins $l = 1 - 8$.

Here we have assumed the B-mode angular power spectrum to be exactly zero. The normalisation factor is defined as

$$N_l = \ln(\ell_{\text{up},l}) - \ln(\ell_{\text{dn},l}), \quad (6)$$

with the bin-ranges designated by $\ell_{\text{up},l}$ and $\ell_{\text{dn},l}$, respectively.

The band window functions are illustrated in Fig. 2 of Joachimi et al. (2021). The same reference also provides the exact functional form of each window. Qualitatively, all band windows above $\ell \sim 500$ resemble tophat filters, while for smaller multipole-values, they are closer to Gaussian filters. In practice, using band powers instead of the angular power spectrum for the theory pipeline only has a very minor effect on the resulting parameter contours.

The angular power spectrum for the auto and cross-correlation is obtained using the Limber approximation

$$C_{ij}(\ell) = \int_0^{\chi_H} \frac{g_i(\chi)g_j(\chi)}{\chi^2} P_{\text{full-physics}}\left(\frac{\ell}{\chi}, z(\chi)\right) d\chi, \quad (7)$$

with the co-moving distance χ going from 0 to the horizon χ_H . The power spectrum $P_{\text{full-physics}}(k, z)$ is given by

$$P_{\text{full-physics}} = S P_{\text{gravity-only}}, \quad (8)$$

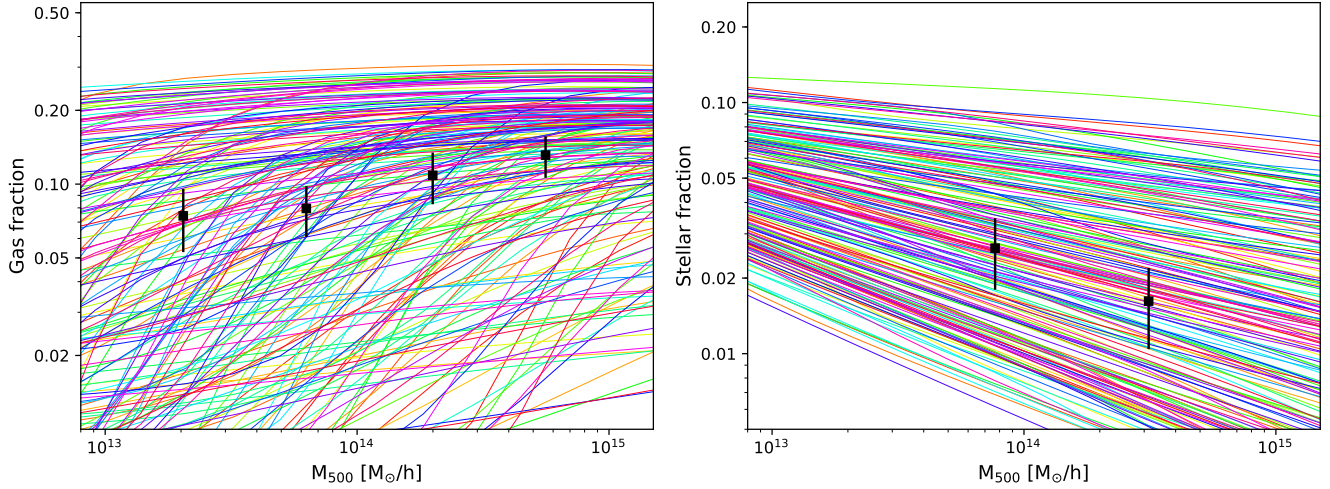


Figure 2. Gas and stellar fractions assuming a Planck cosmology and randomly selected parameter values for the baryonification model (coloured lines). The selected parameters are identical to the ones shown in Fig. 1 randomly sampling the prior range of the baryonic emulator. The data points correspond to binned X-ray and optical measurements from individual galaxy groups and clusters (see [Giri & Schneider 2021](#)). The mass unit M_{500} consists of the estimated X-ray mass at the radius r_{500} assuming hydrostatic equilibrium.

where $P_{\text{gravity-only}}$ is obtained using the revised halo fit predictor from [Takahashi et al. \(2012\)](#) and the multiplicative baryonic suppression factor $\mathcal{S}(k, z)$ is calculated with the baryonic emulator from [Giri & Schneider \(2021\)](#). Note that \mathcal{S} depends on cosmology via the cosmic baryon fraction $f_b \equiv \Omega_b/\Omega_m$, which is emulated together with the seven parameters of the baryonification model¹.

The lensing weights are given by

$$g_i(\chi) = \frac{3\Omega_m}{2} \left(\frac{H_0}{c} \right)^2 \chi(1+z) \int_{\chi(z)}^{\chi_H} n_i(z) \frac{\chi(z') - \chi(z)}{\chi(z')} dz', \quad (9)$$

where $n_i(z)$ is the galaxy distribution at redshift bin i . The galaxy redshift distributions are obtained from the KiDS 1000 data release (see Fig. 2 in [Asgari et al. 2021](#)). The calculations of the weak-lensing band powers are performed using the PyCosmo framework presented in [Refregier et al. \(2018\)](#).

Compared to the original analysis from KiDS 1000, we simplify the analysis pipeline to some degree. First of all, we assume neutrinos to be mass-less. While it is known that at least two of the three neutrino flavour states have small but nonzero mass, it has been shown by [Hildebrandt et al. \(2020\)](#) that massive neutrinos only lead to very minor changes of the posterior contours for the KiDS 450 data. Second, we use the revised halo fit routine from [Takahashi et al. \(2012\)](#) together with the [Eisenstein & Hu \(1998\)](#) linear transfer function instead of the HMcode ([Mead et al. 2015](#)) combined with Class ([Blas et al. 2011](#)). While [Joachimi et al. \(2021\)](#) have reported a $0.3\text{-}\sigma$ shift of the S_8 parameter between HMcode and halo fit, we do not find such a large deviation between the two cases. Finally, we assume a fixed shift of the galaxy redshift distribution functions, following the findings of ([Asgari et al. 2021](#), see their Table 1), but we do not vary the mean of the redshift distributions as performed in the standard KiDS analysis. Keeping all $n_i(z)$ values fixed allows us to reduce the number of variables by 5. We have checked that including the fixed shifts in redshift distribution only has a minor effect on the resulting S_8 posteriors.

In Fig. 1 we plot 200 angular power spectra with varying baryonic

model parameters (and fixed cosmology to the Planck values) as coloured lines. The baryonic parameters have thereby been assigned randomly within the prior ranges given by the baryonic emulator of [Giri & Schneider \(2021\)](#), see also Table 1). These prior ranges are selected to be significantly broader than all known results from hydrodynamical simulations. The spread of the coloured lines therefore provides a conservative estimate for the maximum uncertainty from baryonic feedback on the weak-lensing signal. Note that in Fig. 1, the observed band power values (black symbols) are plotted together with the predicted angular power spectra (coloured lines). Although not exactly the same, both measures remain within a few percent from each other, a shift that is not visible in the plot.

3.2 X-ray gas and stellar fractions

As mentioned above, the baryonification model can be used to recover the baryonic suppression of the matter power spectrum based solely on information about the halo gas profiles (see e.g. [Schneider et al. 2019](#); [Aricò et al. 2021](#); [Giri & Schneider 2021](#)). For example, it is possible with X-ray data to obtain detailed information about the gas content within the virial radius of galaxy groups and clusters. Furthermore, X-ray observations can be used to estimate the total halo mass (with the assumption of hydrostatic equilibrium). Combining weak-lensing data with X-ray observations can therefore help to provide information about baryonic effects and lead to improved constraints for cosmological parameters ([Schneider et al. 2020b](#)).

In this paper we will use the binned X-ray gas and stellar fractions presented in [Giri & Schneider \(2021\)](#). The data is built upon individual measurements of the gas and stellar content of galaxy groups and clusters from various different Refs. ([Vikhlinin et al. 2009](#); [Gonzalez et al. 2013](#); [Sanderson et al. 2013](#); [Lovisari et al. 2015](#); [Kravtsov et al. 2018](#)). The binned data is shown as black symbols in Fig. 2 with the gas fraction to the left and the stellar fraction to the right. Both fractions show a clear trend as a function of halo mass (M_{500}). Galaxy groups and small clusters are lacking gas compared to large clusters, where the gas fraction approaches the mean cosmological fraction $f_g = \Omega_b/\Omega_m - f_{\text{star}}$. For the stellar component, the trend

¹ All other cosmological parameters have a negligible effect on the baryonic suppression signal \mathcal{S} (as shown in [Schneider et al. 2020a](#)).

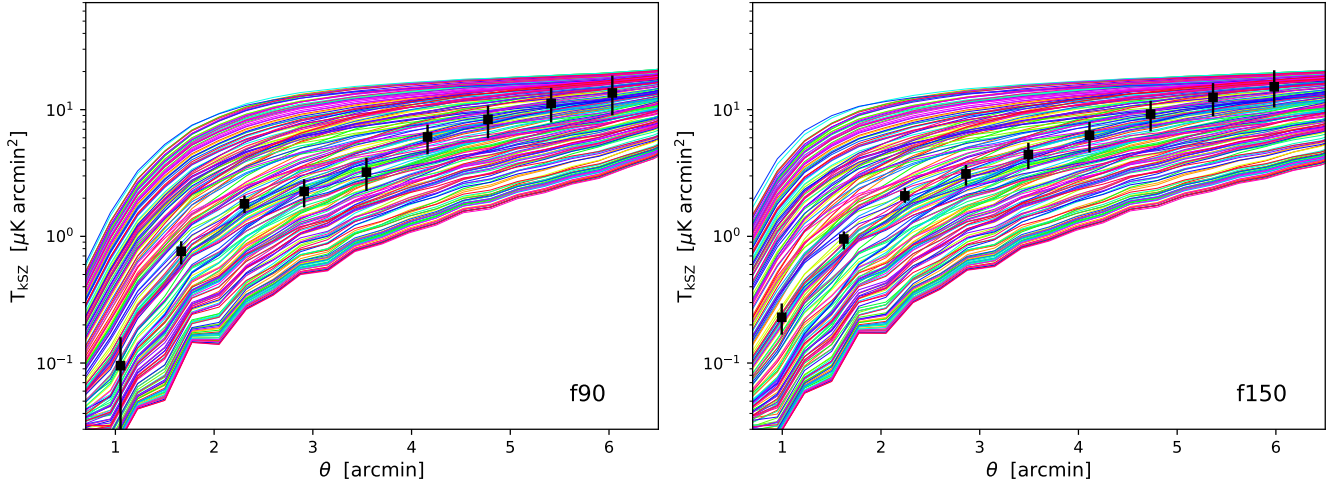


Figure 3. Stacked kSZ profiles from ACT at 98 GHz (f90, left-hand panel) and 150 GHz (f150, right-hand panel) at $z = 0.55$ (black data points). The coloured lines correspond to the predicted kSZ profiles for a halo with $M_{200} = 3 \times 10^{13} M_{\odot}$ assuming a fixed Planck cosmology and randomly varying parameters of the baryonification model. The predictions correspond to the same models shown in Fig. 1 and 2, providing a conservative estimate for the maximum variation due to baryonic feedback processes.

is reversed with a rising total stellar fraction towards smaller halo masses.

For the prediction of the X-ray gas and stellar fractions, we use the stellar, gas and halo masses of the baryonification model, i.e.,

$$f_{\chi} = \frac{M_{\chi}(r_{500})}{(1 + b_{\text{hse}})M_{\text{tot}}(r_{500})}, \quad (10)$$

with $\chi = \{\text{gas}, \text{star}\}$ and where r_{500} is the radius corresponding to a mean halo density of 500 times the critical density of the universe. In Eq. (10) we have introduced the hydrostatic bias b_{hse} that accounts for deviations from hydrostatic equilibrium due to in-falling gas in the outskirts of haloes. We use b_{hse} as an additional model parameter assuming a Gaussian prior with a mean of 0.26 and a standard deviation of 0.07 (Hurier & Angulo 2018). This assumption is based on an analysis of CMB data and agrees well with other direct estimates from X-ray and lensing observations (see e.g. Fig. 10 in Salvati et al. 2018).

The predicted gas and stellar fractions for different baryonic parameters (at fixed cosmology) are shown in Fig. 2 as coloured lines. The model parameters are the same than in Fig. 1 and have been selected randomly within the prior ranges provided in Table 1. The potential of X-ray data to constrain baryonic parameters becomes evident when comparing the errors of the data points in Fig. 2 to the widely spread predictions from the baryonification model.

3.3 Profiles from the kinematic Sunyaev-Zeldovich effect

Another promising observable of the gas around haloes arises from the Sunyaev-Zeldovich effect (SZ, Sunyaev & Zeldovich 1970, 1972). The predominant process is the thermal SZ (tSZ), a spectral distortion of the CMB black-body spectrum due to inverse Compton scattering of the CMB photons by the hot free electrons in galaxy clusters, which is proportional to the integrated electron pressure along the line of sight. Very recently, Gatti et al. (2021) and Tröster et al. (2021) have published first result of tSZ measurements cross-correlated with weak-lensing data from DES and KiDS, respectively. They have shown that such cross-correlation studies can be used to simultaneously constrain cosmology and baryonic feedback parameters.

In this paper we focus instead on the kSZ effect, consisting of an up-scattering of the CMB photons due to the bulk motion of the free electrons in galaxy groups and clusters. This is proportional to the integrated electron momentum along the line of sight, therefore, if the velocity is known, it provides a direct measurement of the electron density, as opposed to the tSZ which depends also on the electron temperature. For this reason, the kSZ effect is a better probe of lower density environments compared to the tSZ and X-ray measurements, such as the regions further away from the halo centre and smaller halo masses. We use kSZ measurements from the Atacama Cosmology Telescope (ACT) DR5 and Planck (Schaan et al. 2021; Amodeo et al. 2021) obtained for the CMASS galaxy sample from the Baryon Oscillation Spectroscopic Survey (BOSS, Ahn et al. 2014), having average halo mass and redshift of $M_{200} = 3 \times 10^{13} M_{\odot}$ and $z = 0.55$.

The kSZ temperature measured within a disc of radius θ around a galaxy group or cluster is given by the relation

$$T_{\text{kSZ}}(\theta) = T_{\text{CMB}} \left(\frac{v_{e,r}}{c} \right) \tau_{\text{gal}}(\theta), \quad (11)$$

where τ_{gal} is the Thomson optical depth and $v_{e,r}$ is the free electron bulk line-of-sight velocity, approximated as $v_{e,r} = 1.06 \times 10^{-3} c$ (Schaan et al. 2021; Amodeo et al. 2021). The optical depth is obtained via a line-of-sight integral over the electron number density profile, i.e.,

$$\tau_{\text{gal}}(\theta) = 2\sigma_T \int_0^{\infty} n_e \left(\sqrt{l^2 + d_A(z)^2 \theta^2} \right) dl, \quad (12)$$

with σ_T being the Thomson scattering cross-section and $d_A(z)$ the angular diameter distance. The electron density $n_e(r)$ is related to the gas profile via

$$n_e(r) = \frac{(X_H + 1)}{2m_{\text{amu}}} \rho_{\text{gas}}(r), \quad (13)$$

with the hydrogen mass fraction $X_H = 0.76$ and the atomic mass unit m_{amu} . Note that the gas profile $\rho_{\text{gas}}(r)$ is directly obtained from the baryonification model and contains both the one-halo and the two-halo term.

In order to compare the kSZ temperature to observations from the ACT survey, we convolve Eq. (11) with the beam profile measured

at 98 and 150 GHz (called f90 and f150). These beam profiles are assumed to be of Gaussian shape (with FWHM = 2.1 and 1.3 arcmin for f90 and f150, respectively) which has shown to be a good approximation (see Fig. 5 of [Schaan et al. 2021](#)). Finally, we smooth the data using a step-like filter function that is 1 within δ_d , -1 between δ_d and $\sqrt{2}\delta_d$, and 0 otherwise (see Eq. 9 of [Schaan et al. 2021](#)). Applying this filter is necessary to reproduce the aperture photometry filtering used for the data.

In Fig. 3, we show the predicted kSZ profiles assuming a host halo of $M_{200} = 3 \times 10^{13} M_\odot$ at $z = 0.55$ (coloured lines). The different models are characterised by randomly varying parameters of the baryonification model (at fixed cosmology). They consist of the same models shown in Fig. 1 and 2, covering the full prior range of the baryonic parameters given in Table 1 (which is a conservative estimate for the maximum variation of the baryonic feedback processes). Note that although the kSZ signal is independent of frequency, distinct profiles are measured due to the different beams at 98 GHz (f90) and 150 GHz (f150), shown in the left- and right-hand panels, respectively.

The black data points in Fig. 3 show the stacked kSZ signal from the Atacama Cosmology Telescope (ACT) at 98 and 150 GHz ([Schaan et al. 2021](#)). The stacking was performed by cross-correlating the ACT signal with the CMASS galaxy catalogue. The corresponding galaxies that appear in both data-sets have a mean stellar mass of $M_{\text{star}} \sim 3 \times 10^{11} M_\odot$ which corresponds to a halo mass of $M_{200} \sim 3 \times 10^{13} M_\odot$ assuming the abundance matching estimate of [Kravtsov et al. \(2018\)](#).

For the inference analysis performed in this paper, note that we do not assume a fixed value for the halo mass but we keep M_{200} as a free model parameter (within the prior limits given in Table 1). Furthermore, we account for the fact the error-bars of the stacked profiles from ACT are strongly correlated by including the error covariances (see Fig. 7 of [Schaan et al. 2021](#)).

Fig. 3 shows that the variations in the shape and amplitude of kSZ profiles from different feedback parameters widely exceeds the size of the error-bars from the ACT observations. This illustrates the great potential of kSZ data to provide constraints on the strength of baryonic feedback.

4 RESULTS

Based on the data and the theory pipeline discussed above, we now perform an inference analysis using the Markov Chain Monte Carlo (MCMC) sampling method. We thereby simultaneously vary five cosmological parameters ($\Omega_m, \Omega_b, \sigma_8, n_s, h_0$), seven baryonic parameters ($M_c, \mu, \theta_{\text{ej}}, \delta, \gamma, \eta, \eta_\delta$), and one parameter accounting for intrinsic alignment (A_{IA}). Whenever we include X-ray and/or kSZ data, we furthermore vary the hydrostatic bias parameter (b_{hse}) and/or the halo mass parameter of the kSZ profile (M_{200}). A list of all parameters including their prior ranges are provided in Table 1.

As a first step, we produce MCMC samples based only on the weak-lensing band power from the KiDS-1000 data release ([Asgari et al. 2021](#)). We investigate two scenarios, one where we ignore all baryonic effects and one where we include the full baryonification model. Note that the former is only added to illustrate the effect of baryonic feedback on the posterior contours and should not be regarded as physically viable scenario.

As a further step, we combine the weak-lensing band-power data with the mean X-ray cluster gas (and stellar) fractions ([Giri & Schneider 2021](#)) and with the stacked kSZ profiles at 98 and 150 GHz ([Schaan et al. 2021](#)). For these scenarios, we only investigate mod-

Parameter name	Acronym	Prior range
Matter abundance	Ω_m	[0.1, 0.6]
Baryon abundance	Ω_b	[0.04, 0.06]
Clustering amplitude	σ_8	[0.3, 1.3]
Hubble parameter	H_0	[0.64, 0.82]
Spectral index	n_s	[0.84, 1.10]
<hr/>		
Intrinsic alignment parameter	A_{IA}	[0, 2]
<hr/>		
First gas parameter (Eq. 2)	$\log_{10} M_c$	[11, 15]
Second gas parameter (Eq. 2)	μ	[0, 2]
Third gas parameter (Eq. 2)	θ_{ej}	[2, 8]
Fourth gas parameter (Eq. 2)	γ	[1, 4]
Fifth gas parameter (Eq. 2)	δ	[3, 11]
First stellar parameter (Eq. 4)	η	[0.05, 0.4]
Second stellar parameter (Eq. 4)	η_δ	[0.05, 0.4]
<hr/>		
Hydrostatic mass bias (Eq. 10)	b_{hse}	0.26 ± 0.07
<hr/>		
Total halo mass (for kSZ profiles)	M_{200}	[1e13, 4e13]

Table 1. List of MCMC parameters separated into cosmological, intrinsic alignment, baryonic, hydrostatic bias, and kSZ halo mass parameters (top to bottom). We use a Gaussian prior for b_{hse} and flat priors for all other parameters.

els including the full baryonification model, as the data is primarily added to provide further constraints on the baryonic parameters.

In the following sections, we discuss the outcome of the MCMC analyses, focusing first on the baryonic and then on the cosmological parameters. Finally, we also provide a observation-based estimate for the baryonic suppression of the matter power spectrum, and we compare it to predictions from the most recent hydrodynamical simulations.

4.1 Constraining the baryonification model

As a first result, we provide constraints for the baryonification model parameters. In Fig. 4, the posterior contours from the KiDS-1000 WL band-power alone (red) are compared to the contours from the combined WL + Xray + kSZ data-set (dark cyan). The results from the data combinations WL + Xray and WL + kSZ are shown in Fig. B1 of Appendix B.

Fig. 4 shows that the WL band-power data alone is unable to constrain the baryonic model parameters very well. Only the M_c , θ_{ej} , and η parameters show a slight preference for small values without, however, excluding larger values either. The other parameters yield fairly flat distributions without preference for any particular value within the prior ranges.

Not surprisingly, the combined WL + Xray + kSZ data vector leads to stronger constraints on the baryonic parameters. Especially M_c , μ , and η are well constrained, while δ and η_δ are pushed towards the lower end of the prior range. Only the remaining parameters θ_{ej} and γ remain unconstrained by the WL + Xray + kSZ data combination. A comparison with Fig. B1 reveals that the constraints on the stellar parameters η and η_δ are entirely driven by the X-ray fractions that contain information about the stellar abundance in haloes. The posteriors of the gas parameters M_c , μ , and δ , on the other hand, are a product of combining both X-ray and kSZ data.

Fig. 4 illustrates the potential of current and future gas observations to constrain baryonic feedback effects relevant for cosmology. In the future, combining e.g. observations from Euclid ([Laureijs et al. 2011](#)) with X-ray data from eROSITA ([Merloni et al. 2012](#)) and

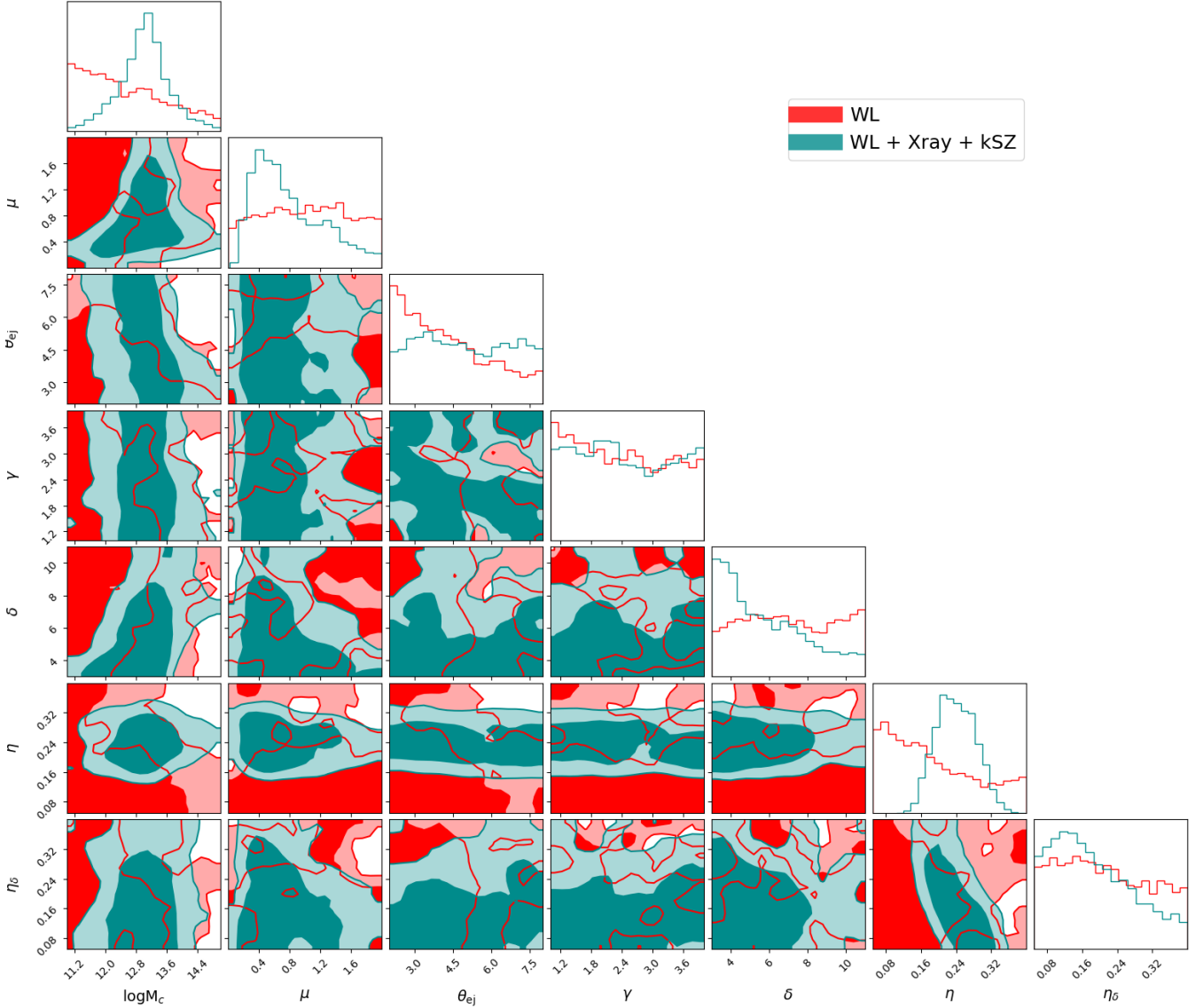


Figure 4. Posterior contours of the baryonification model parameters at 68 and 95 percent confidence level. Results based on the weak-lensing (WL) band-power data from KiDS 1000 (Asgari et al. 2021) are shown in red colour. Results from the combined data set including KiDS 1000 WL data, X-ray gas (and stellar) fractions from Giri & Schneider (2021), and stacked kSZ profiles from ACT (Schaan et al. 2021) are shown in dark cyan colour. Posterior contours from the WL+Xray and WL+kSZ data combinations are provided in Fig. B1.

SZ measurements from CMB-S4 (Abazajian et al. 2016) will make it possible to further decrease the current uncertainties related to the baryonification model. In Schneider et al. (2020b) it is shown that combining Euclid weak-lensing observations with X-ray data from eROSITA will make baryonification model errors shrink by more than an order of magnitude. As a consequence, we expect baryonic nuisance parameters to not substantially degrade cosmological parameter estimates, provided external data from X-ray or the SZ effect are included.

4.2 Constraining cosmological parameters

Arguably the most intriguing result from the recent weak-lensing surveys CFHTLenS, KiDS, DES, and HSC is the mild yet persistent tension with the matter abundance (Ω_m) and clustering amplitude (σ_8) measured by the CMB satellite Planck. The tension is usually

quantified in terms of the combined S_8 parameter, defined as

$$S_8 \equiv \sigma_8 \sqrt{\Omega_m / 0.3}. \quad (14)$$

In this section, we investigate the S_8 -tension in connection with the baryonic suppression effects.

The left-hand panel of Fig. 5 illustrates the Ω_m and S_8 posterior contours (at 68 and 95 percent level) based on the WL band power data from KiDS 1000 (Asgari et al. 2021). The black contours correspond to the case where baryonic effects are ignored in the prediction pipeline (which means that the baryonic power suppression function $S \equiv 1$ at all scales and redshifts). The red contours correspond to the model where all 7 parameters of the baryonification model are varied (and marginalised over). In green we show the contours obtained from the TT, TE, EE + lowE data combination of the Planck legacy analysis (Aghanim et al. 2020a). The plot confirms the tension between the WL shear and the CMB measurements highlighted by the

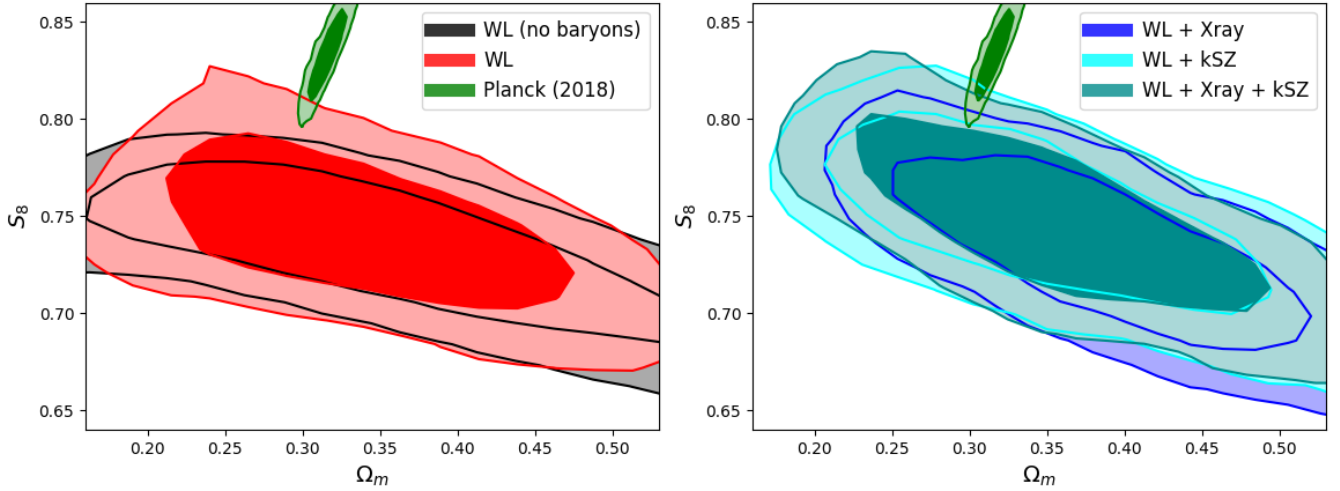


Figure 5. Constraints on the cosmological parameters σ_8 and Ω_m (left-hand panel) and on the combined $S_8 = \sigma_8 \sqrt{\Omega_m/0.3}$ parameter (right-hand panel). The black and red posterior contours show results from weak-lensing data alone, assuming no baryonic effects and marginalising over all baryonification parameters. Results from the combined analysis including weak-lensing and X-ray gas fraction and kSZ profiles data are again shown in blue and cyan. The green contours correspond to CMB estimates from Planck. All posteriors are shown at 68 and 95 percent confidence level, respectively.

KiDS science team in [Asgari et al. \(2021\)](#). It also illustrates the need for a realistic modelling of baryonic feedback. Including baryonic nuisance parameters leads to a broadening of the contours in the S_8 direction, thereby slightly alleviating the S_8 -tension with the CMB.

In the right-hand panel of Fig. 5 we show the Ω_m and S_8 posterior contours for the cases where the WL band-power data is combined with observations from X-ray and the kSZ effect. In blue we show the results from the WL + Xray data combination. They are very similar to the results from the WL only case (red). In cyan we provide the contours from the WL + kSZ data. Compared to the contours from the WL only and the WL + Xray cases, they are slightly shifted in the direction of the Planck results. The dark-cyan contours finally show the results from the full WL + X-ray + kSZ data combination. In terms of the S_8 -tension, it provides limits that are similar to the WL + kSZ case. We conclude that, while baryonic feedback visibly affects the posterior contours in the Ω_m - S_8 plane, it is unable to fully solve the S_8 tension. This verdict based on WL shear is in qualitative agreement with the recent findings from galaxy-galaxy lensing ([Leauthaud et al. 2017](#); [Lange et al. 2021](#); [Amodeo et al. 2021](#)).

The original S_8 parameter defined in Eq. (14) is not perfectly orthogonal to the degeneracy trend between the Ω_m and σ_8 parameters. A more optimal match is obtained by the parameter

$$\Sigma_8 \equiv \sigma_8 (\Omega_m/0.3)^\alpha, \quad (15)$$

with best-fitting value $\alpha = 0.58$ ([Asgari et al. 2021](#)). For an approximate, single-parameter comparison of the tension between WL shear and the CMB data, it is therefore advisable to use Σ_8 instead of the original S_8 parameter.

In Fig. 6 we illustrate the one dimensional constraints on the Σ_8 parameter. While the left-hand panel shows the maximum likelihood values with error-bars displaying the 68 percent confidence ranges, the right-hand panel provides the full posterior distributions. The colours are the same than in the previous plots (WL only results with and without baryonic effects in red and black, WL + Xray results in blue, WL + kSZ results in cyan, WL + Xray + kSZ results in dark cyan, and CMB results in green).

Assuming Gaussian distributions (which is not an unreasonable

assumption, see right-hand panel of Fig. 6), we apply a simple measure to quantify the tension between the different data-sets given by $|\mu_A - \mu_B|/(\sigma_A + \sigma_B)^{1/2}$, where $\{\mu_A, \mu_B\}$ correspond to the means and $\{\sigma_A, \sigma_B\}$ to the variances of the distributions $\{A, B\}$. With this measure, we find the WL data alone to be in 3.75σ tension with the Planck measurement if baryonic effects are ignored. This tension is reduced to 3.19σ if baryonic effects are included and marginalised over. For the WL + Xray and WL + kSZ data combinations, we find a tension of 3.08 and 2.82σ , respectively. Finally, the tension of the full WL + Xray + kSZ data set with the CMB observations from Planck is also at 2.82σ .

The comparison of the Σ_8 posteriors shows that ignoring baryonic feedback in the modelling pipeline leads to a bias of about half a standard deviation compared to the case where baryonic effects are included and marginalised over. Including additional information from X-ray and kSZ observations pushes the distribution towards models with strong feedback effects, further reducing the tension with Planck by about half a standard deviation. We again conclude that, while baryonic feedback models may induce a slight reduction of the tension between WL shear data and CMB observations, they cannot fully reconcile the two data-sets.

Note again that for the analysis presented above, we use a different pipeline than the KiDS science team and we therefore obtain slightly different results than [Asgari et al. \(2021\)](#). A comparison at the level of the Ω_m and S_8 contours is provided in Appendix. A.

4.3 Constraining the matter power spectrum

In this section we take a closer look at the baryonic suppression signal of the matter power spectrum. While current hydrodynamical simulations largely agree on the spoon-like shape of this suppression, there is a considerable scatter between the different predictions from simulations (e.g. [Chisari et al. 2019](#); [Huang et al. 2019](#)). The differences are a result of the various feedback implementation and calibration strategies.

[Giri & Schneider \(2021\)](#) has shown that the baryonification method is able to recover the power suppression from baryonic effects based solely on observed properties of the halo profiles. It is therefore

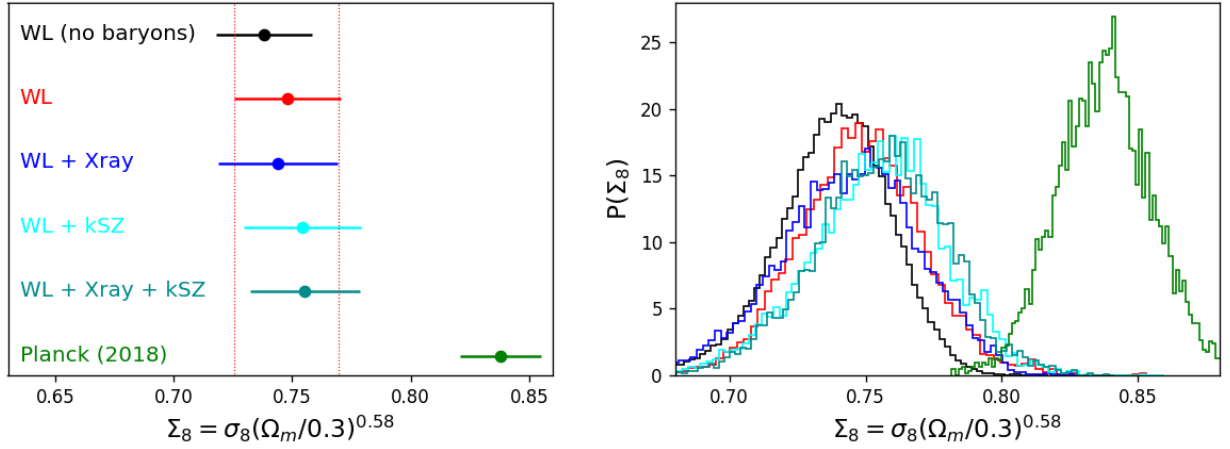


Figure 6. Posterior distribution of the combined $\Sigma_8 = \sigma_8(\Omega_m/0.3)^{0.58}$ parameter which is orthogonal to the Ω_m - σ_8 degeneracy line. The left- and right-hand panels show the maximum likelihoods with 68 percent errors and the full distributions, respectively. The results based on the WL data alone are shown in grey and red (without and with baryonic suppression effect), from the WL + Xray and WL + kSZ data in blue and cyan, and from WL + Xray + kSZ in dark cyan.

possible to take advantage of the X-ray, kSZ, and (via the Limber approximation) the WL band power observations to predict the true amplitude and shape of the baryonic power suppression (a method also suggested in [Aricò et al. 2020](#)). This information can then be used to assess the validity of hydrodynamical simulations or to exclude biases affecting other cosmological probes based on the power spectrum (such as e.g the galaxy correlation).

In the top-panels of Fig. 7 we plot the constraints on the baryonic power suppression signal at 68 and 95 percent confidence level. The leftmost panel shows the results from the WL band power alone (red), the second and third panels illustrate the results from the combined WL + Xray (blue) and WL + kSZ (cyan) data sets, and the rightmost panel corresponds to the combined WL + Xray + kSZ data vector (dark cyan). Note that these constraints include uncertainties related to baryonic, intrinsic-alignment, and cosmological parameters.

The constraints from the WL band power alone (first top-panel of Fig. 7) are rather loose. While they hint towards a suppression of the power spectrum, they do not exclude cases where baryons induce a net boost of power instead of a downturn. Considering wave-modes below $k = 10$ h/Mpc, the smallest and largest values of the suppression factor at 95 percent confidence level are $S = 0.64$ and $S = 1.27$, respectively. Note that these findings are in qualitative agreement with [Yoon & Jee \(2021\)](#).

The combined WL and X-ray data set (second top-panel of Fig. 7) leads to a stronger baryonic suppression signal compared to the WL observations alone. Models with a net power boost (and no sign of suppression) can be excluded at 68 (but not at 95) percent confidence. The smallest wave-mode where the baryonic feedback yields a suppression beyond one percent lies between $k_{\min} = 0.12$ and 1.90 h/Mpc. The largest amplitude of the suppression signal (where S is at its minimum) lies in the range $S_{\min} = 0.77 - 0.97$. Both measurements are provided at the 68 percent confidence level.

The results based on the combined WL and kSZ data (third top-panel of Fig. 7) show the strongest suppression signal. This should not come as a surprise, as the contours of the Ω_m - S_8 plane (shown in Fig. 5) indirectly hint towards a strong feedback suppression signal. For the WL + kSZ setup, we can exclude scenarios with a boost (and no net downturn) at more than 95 percent confidence. The smallest wave-mode where the baryonic suppression signal exceeds one percent lies within the range $k_{\min} = 0.11 - 0.42$ h/Mpc. The largest amplitude of the suppression signal is constrained to be within

$S_{\min} = 0.67 - 0.88$. Both measures again correspond to the 68 percent confidence level.

Finally, the right-most top-panel of Fig. 7 shows the baryonic power suppression from the combined WL + Xray + kSZ data. The resulting suppression signal is closest to the one from the WL + kSZ case. At the 68 percent confidence level, S exceeds one percent above $k_{\min} = 0.1 - 0.5$ h/Mpc and reaches a minimum value of $S_{\min} = 0.70 - 0.90$ at $k \sim 8$ h/Mpc.

For now, we have provided estimates of the baryonic power suppression assuming no prior knowledge on cosmology. Fixing the cosmological parameters will inevitably reduce the uncertainties illustrated in Fig. 7. This is especially true regarding the cosmic baryon fraction $f_b = \Omega_b/\Omega_m$, which has been shown to directly affect the baryonic suppression signal. Other cosmological parameters have a negligible effect on the amplitude of the suppression S (see [Schneider et al. 2020a](#)).

Now we multiply the posterior distribution with a uniform prior of $0.15 < f_b < 0.17$. The prior range is selected so that it comfortably includes the best fitting cosmologies of WMAP and Planck. This allows us to obtain results that can be directly compared to various hydrodynamical simulations which are all based on either WMAP or Planck cosmologies. Note that, in principle, the WL + Xray + kSZ data-set could be combined with the full data vector from Planck (instead of only assuming a CMB-informed prior on f_b). We refrain from doing so because the internal tension between these two data sets would push the parameter values towards very strong feedback models potentially biasing our conclusions.

The resulting estimates for the baryonic power suppression are plotted in the bottom-panels of Fig. 7. As expected, adding a prior on the cosmic baryon fraction leads to a tightening of the uncertainty contours. The effect is most prominent for the WL + Xray and the full WL + Xray + kSZ data combination. The reason for this tightening is the data from the X-ray gas fractions which directly depends on the f_b parameter. Once f_b is constricted to a narrow range, the gas fractions provide much stronger constraints on the baryonification model.

Based on the data shown in the bottom-panels of Fig. 7, we now quantify the constraints on the baryonic suppression signal in terms of scale and amplitude. For the smallest wave-mode (k_{\min}) where S falls below 0.99, we obtain $k_{\min} = 0.11 - 0.32$ ($0.1 - 0.8$) h/Mpc for WL + Xray, $k_{\min} = 0.11 - 0.35$ ($0.1 - 1.8$) h/Mpc for WL + kSZ,

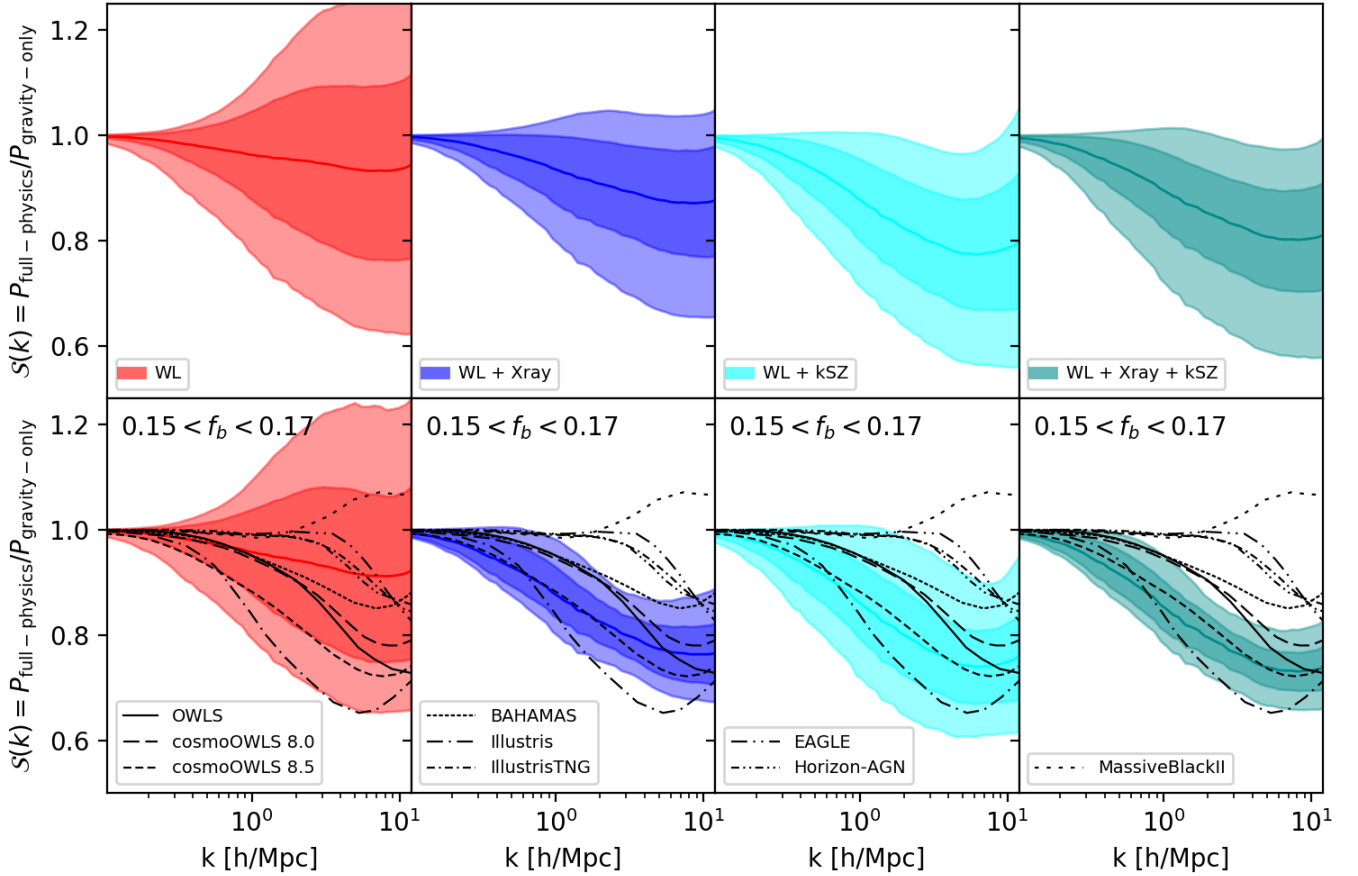


Figure 7. Constraints on the baryonic suppression of the matter power spectrum from weak-lensing (WL) alone, WL plus X-ray fractions (Xray), WL plus stacked profiles from the kSZ, and the full data vector WL + Xray + kSZ (from left to right). All contours are shown at 68 and 95 percent confidence level. *Top-panels:* All cosmological, baryonic, and intrinsic alignment parameters are marginalised over. *Bottom-panels:* Only models with a cosmic baryon fraction ($f_b \equiv \Omega_b/\Omega_m$) inside the range $0.15 < f_b < 0.17$ are included into the analysis. This range comfortably includes all WMAP and Planck cosmologies and allows for a direct comparison with recent hydrodynamical simulations which are all based on either Planck or WMAP (black lines).

and $k_{\min} = 0.11 - 0.25$ ($0.1 - 0.55$) h/Mpc for WL + Xray + kSZ at the 68 (95) percent confidence level. For the minimum value of the baryonic suppression signal (S_{\min}) we get $S_{\min} = 0.71 - 0.82$ ($0.67 - 0.87$) for WL + Xray, $S_{\min} = 0.67 - 0.81$ ($0.61 - 0.90$) for WL + kSZ, and $S_{\min} = 0.69 - 0.77$ ($0.66 - 0.81$) for the combined WL + Xray + kSZ data set, again at 68 (95) percent confidence level. Finally, we notice that the f_b -prior on the cosmic baryon fraction has only little influence on the results from the WL only case (dark red, left-hand panel). While a slight tightening of the contours is visible, it is not enough to draw conclusions that are significantly different from the ones obtained without further assumptions regarding the cosmic baryon fraction.

The black lines in the bottom-panels of Fig. 7 correspond to the predicted baryonic power suppression signal from various hydrodynamical simulations. We show the results from OWLS (solid, Schaye et al. 2010; van Daalen et al. 2011), cosmo-OWLS 8.0 and 8.5 (long dashed and short dashed, Le Brun et al. 2014; Mummery et al. 2017), BAHAMAS (dotted, McCarthy et al. 2017), Illustris (long dash-dotted, Vogelsberger et al. 2014), IllustrisTNG (short dash-dotted, Springel et al. 2018), EAGLE (long dash-double-dotted, Schaye et al. 2015; Hellwing et al. 2016), H-AGN (short dash-double-dotted, Dubois et al. 2014; Chisari et al. 2018), and MassiveBlackII

(long dotted, Khandai et al. 2015). All simulations except Illustris predict a baryonic power suppression signal in agreement with the WL only data from KiDS. The situation is very different when compared to the WL + Xray data set, where all simulations except OWLS and cosmo-OWLS, are outside of the 95 percent confidence region. From the simulations that disagree, all except Illustris show milder suppression signals than suggested by the WL + Xray data. The best match is obtained by cosmo-OWLS 8.5 which stays within the 68 percent confidence region over all scales investigated.

More simulations agree with the analysis based on the less constraining WL + kSZ data set. While it is again only the cosmo-OWLS 8.5 simulation that stays within the 68 percent confidence region over all scales, the majority of simulations stay within the 95 percent region. Exceptions are IllustrisTNG, EAGLE, H-AGN, and MassiveBlackII that yield a milder suppression signal than suggested by the WL + kSZ data.

The full WL + Xray + kSZ data set shows a very similar behaviour than the WL + Xray case. Again, it is only the cosmo-OWLS 8.5 simulation that is in full agreement with the data. All other simulations lie partially outside the 95 percent confidence region.

It is interesting to note that the BAHAMAS simulation (McCarthy et al. 2017), which has been specifically calibrated to data from X-ray

gas fractions, lies (slightly) outside our 95 percent confidence area for the WL + Xray case. We speculate that this could be due to the hydrostatic mass bias from (Hurier & Angulo 2018) that has been obtained from CMB observations. This direct estimate is somewhat larger than what is typically found in hydrodynamical simulations and could lead to an increase in amplitude of the baryonic suppression signal. Another possibility are resolution effects leading to an artificial increase of the BAHAMAS results. Such an effect has been reported in van Daalen et al. (2020) and could, at least somewhat, solve the discrepancy shown in the bottom-panels of Fig. 7.

We conclude that the WL band-power data from KiDS 1000 alone provides little constraining power on the baryonic feedback effects (a finding in qualitative agreement with e.g. Fluri et al. 2019; Huang et al. 2021; Yoon & Jee 2021; Tröster et al. 2021). Combining weak-lensing observations with data from X-ray gas fraction and from kSZ profiles leads to much stronger constraints that strongly disagree with simulations that predict mild feedback effects, such as EAGLE, IllustrisTNG, H-AGN or MassiveBlackII.

Finally, our analysis highlights the need to include baryonic feedback effects in any cosmological analysis pipeline which is based on the matter power spectrum beyond $k \sim 0.1$ h/Mpc. This includes in particular spectroscopic and photometric galaxy clustering observations, maps of the X-ray or SZ signal, or low-redshift observations from radio interferometres.

5 CONCLUSIONS

In this paper we carry out an independent analysis of the KiDS-1000 weak lensing (WL) band power measurements and we combine, for the first time, WL data with observations from X-ray gas (and stellar) fractions and with stacked gas profiles from the kSZ effect. We thereby specifically focus on the influence of baryonic feedback processes, which are modelled using the baryonification method and assuming seven free parameters.

There are three main questions we attempt to answer with the present paper: (i) how well can we constrain the parameters of the baryonification model with current data? (ii) what does the data tell us about the baryonic suppression of the matter power spectrum? (iii) Does a more general prescription for the baryonic effects alter current constraints on cosmological parameters and can it alleviate the observed S_8 -tension? We are now summarising the answers to these three main questions:

(i) The baryonification model provides a more versatile and generally valid description of baryonic effects compared to what has been used before (such as in the original KiDS analysis). The model contains seven free parameters that can be directly constrained with observations, and it is able to reproduce results from a plethora of different hydrodynamical simulations. We show that the data from the WL band-power alone is unable to constrain the baryonification parameters beyond their prior ranges. Combining weak lensing with X-ray and kSZ observations, on the other hand, allows us to put constraints on five of the seven baryonic parameters.

(ii) Quantifying the baryon-induced suppression of the matter power spectrum (S) is of interest not only for weak lensing but also for other cosmological observations. Furthermore, it can be used as a discriminant of hydrodynamical simulations and their feedback implementation schemes. Assuming the full WL + Xray + kSZ data set and restricting the cosmic baryon fraction to $f_b = 0.15 - 0.17$ (a range that includes both Planck and WMAP cosmologies), we find the minimum of the baryonic suppression signal to be at $S_{\min} = 0.66 - 0.81$, which corresponds to a 19-34 percent baryonic suppression effect

(at 95 percent confidence level). For the largest scale (smallest wave mode k_{\min}) where S deviates from unity by more than one percent, we find $k_{\min} = 0.1 - 0.55$ h/Mpc (at 95 percent confidence level). This corresponds to a significantly larger scale than what is predicted by the majority of hydrodynamical simulations.

(iii) Baryonic feedback processes affect the clustering strength and therefore the observed tension between the KiDS-1000 WL band power measurements and the CMB data from Planck (often referred to as the S_8 -tension). We report the discrepancy between the two data sets to decrease from 3.8 to 3.2σ when baryonic suppression effects are included into the analysis. Furthermore, we find the external X-ray and kSZ data sets to favour strong baryonic feedback. The combined WL + Xray + kSZ data vector yields a remaining tension of 2.8σ with the data from Planck. We conclude that strong baryonic feedback effects may help to alleviate the S_8 tension without, however, fully solving it.

The results from this paper further highlight the importance of including the effects of baryons into the analysis pipelines of modern WL surveys. In the future, we foresee that a combination of WL observations with data from X-ray and the SZ effect will allow us to account for baryonic nuisance parameters without biasing or significantly increasing the errors of cosmological parameters.

ACKNOWLEDGEMENTS

We thank Tilman Troester for his help with the analysis of the KiDS-1000 data. This work is supported by the Swiss National Science Foundation via the grant PCEFP2_181157.

REFERENCES

- Abazajian K. N., et al., 2016, arXiv
- Ade P. A. R., et al., 2016, *Astron. Astrophys.*, 594, A24
- Aghanim N., et al., 2020a, *Astron. Astrophys.*, 641, A6
- Aghanim N., et al., 2020b, *Astron. Astrophys.*, 641, A8
- Ahn C. P., et al., 2014, *Astrophys. J. Suppl.*, 211, 17
- Amodeo S., et al., 2021, *Phys. Rev. D*, 103, 063514
- Amon A., et al., 2021, arXiv e-prints, p. arXiv:2105.13543
- Aricò G., Angulo R. E., Hernández-Montegudo C., Contreras S., Zennaro M., Pellejero-Ibañez M., Rosas-Guevara Y., 2020, *MNRAS*, 495, 4800
- Aricò G., Angulo R. E., Hernández-Montegudo C., Contreras S., Zennaro M., 2021, *Mon. Not. Roy. Astron. Soc.*, 503, 3596
- Asgari M., et al., 2021, *Astron. Astrophys.*, 645, A104
- Bianchini F., et al., 2020, *Astrophys. J.*, 888, 119
- Blas D., Lesgourgues J., Tram T., 2011, *JCAP*, 07, 034
- Chisari N. E., et al., 2018, *Mon. Not. Roy. Astron. Soc.*, 480, 3962
- Chisari N. E., et al., 2019, *Open J. Astrophys.*
- Corasaniti P.-S., Sereno M., Ettori S., 2021, *Astrophys. J.*, 911, 82
- Dubois Y., et al., 2014, *Mon. Not. Roy. Astron. Soc.*, 444, 1453
- Eisenstein D. J., Hu W., 1998, *Astrophys. J.*, 496, 605
- Fluri J., Kacprzak T., Lucchi A., Refregier A., Amara A., Hofmann T., Schneider A., 2019, *Phys. Rev.*, D100, 063514
- Gatti M., et al., 2021, arXiv e-prints, p. arXiv:2108.01600
- Giri S. K., Schneider A., 2021, arXiv e-prints, p. arXiv:2108.08863
- Gonzalez A. H., Sivanandam S., Zabludoff A. I., Zaritsky D., 2013, *Astrophys. J.*, 778, 14
- Hellwing W. A., Schaller M., Frenk C. S., Theuns T., Schaye J., Bower R. G., Crain R. A., 2016, *Mon. Not. Roy. Astron. Soc.*, 461, L11
- Heymans C., et al., 2013, *Mon. Not. Roy. Astron. Soc.*, 432, 2433
- Hikage C., et al., 2019, *Publ. Astron. Soc. Jap.*, 71, 43
- Hildebrandt H., et al., 2017, *Mon. Not. Roy. Astron. Soc.*, 465, 1454
- Hildebrandt H., et al., 2020, *Astron. Astrophys.*, 633, A69

Huang H.-J., Eifler T., Mandelbaum R., Dodelson S., 2019, *Mon. Not. Roy. Astron. Soc.*, 488, 1652

Huang H.-J., et al., 2021, *Mon. Not. Roy. Astron. Soc.*, 502, 6010

Hurier G., Angulo R. E., 2018, *Astron. Astrophys.*, 610, L4

Joachimi B., et al., 2021, *Astron. Astrophys.*, 646, A129

Joudaki S., et al., 2017, *Mon. Not. Roy. Astron. Soc.*, 465, 2033

Khandai N., Di Matteo T., Croft R., Wilkins S., Feng Y., Tucker E., DeGraf C., Liu M.-S., 2015, *Mon. Not. Roy. Astron. Soc.*, 450, 1349

Kravtsov A., Vikhlinin A., Meshcheryakov A., 2018, *Astronomy Letters*, 44, 8

Kuijken K., et al., 2019, *Astron. Astrophys.*, 625, A2

Lange J. U., Leauthaud A., Singh S., Guo H., Zhou R., Smith T. L., Cyr-Racine F.-Y., 2021, *Mon. Not. Roy. Astron. Soc.*, 502, 2074

Laureijs R., et al., 2011, arXiv

Le Brun A. M., McCarthy I. G., Schaye J., Ponman T. J., 2014, *Monthly Notices of the Royal Astronomical Society*, 441, 1270

Leauthaud A., et al., 2017, *Mon. Not. Roy. Astron. Soc.*, 467, 3024

Lovisari L., Reiprich T., Schellenberger G., 2015, *Astronomy & Astrophysics*, 573, A118

McCarthy I. G., Schaye J., Bird S., Le Brun A. M. C., 2017, *Mon. Not. Roy. Astron. Soc.*, 465, 2936

Mead A., Peacock J., Heymans C., Joudaki S., Heavens A., 2015, *Mon. Not. Roy. Astron. Soc.*, 454, 1958

Merloni A., et al., 2012, arXiv

Moster B. P., Naab T., White S. D. M., 2013, *MNRAS*, 428, 3121

Mummery B. O., McCarthy I. G., Bird S., Schaye J., 2017, *Mon. Not. Roy. Astron. Soc.*, 471, 227

Refregier A., Gamper L., Amara A., Heisenberg L., 2018, *Astron. Comput.*, 25, 38

Salvati L., Douspis M., Aghanim N., 2018, *Astron. Astrophys.*, 614, A13

Sanderson A. J., O’Sullivan E., Ponman T. J., Gonzalez A. H., Sivanandam S., Zabludoff A. I., Zaritsky D., 2013, *Monthly Notices of the Royal Astronomical Society*, 429, 3288

Schaan E., et al., 2021, *Phys. Rev. D*, 103, 063513

Schaye J., et al., 2010, *Monthly Notices of the Royal Astronomical Society*, 402, 1536

Schaye J., et al., 2015, *Mon. Not. Roy. Astron. Soc.*, 446, 521

Schneider A., Teyssier R., 2015, *JCAP*, 1512, 049

Schneider A., Teyssier R., Stadel J., Chisari N. E., Le Brun A. M. C., Amara A., Refregier A., 2019, *JCAP*, 03, 020

Schneider A., Stoira N., Refregier A., Weiss A. J., Knabenhans M., Stadel J., Teyssier R., 2020a, *JCAP*, 04, 019

Schneider A., et al., 2020b, *JCAP*, 04, 020

Semboloni E., Hoekstra H., Schaye J., van Daalen M. P., McCarthy I. G., 2011, *MNRAS*, 417, 2020

Springel V., et al., 2018, *Mon. Not. Roy. Astron. Soc.*, 475, 676

Sunyaev R. A., Zeldovich Y. B., 1970, *Ap&SS*, 7, 3

Sunyaev R. A., Zeldovich Y. B., 1972, *Comments on Astrophysics and Space Physics*, 4, 173

Takahashi R., Sato M., Nishimichi T., Taruya A., Oguri M., 2012, *Astrophys. J.*, 761, 152

Teyssier R., Moore B., Martizzi D., Dubois Y., Mayer L., 2011, *Mon. Not. Roy. Astron. Soc.*, 414, 195

Tröster T., et al., 2021, arXiv

Troxel M. A., et al., 2018, *Phys. Rev. D*, 98, 043528

Vikhlinin A., et al., 2009, *Astrophys. J.*, 692, 1033

Vogelsberger M., et al., 2014, *Mon. Not. Roy. Astron. Soc.*, 444, 1518

Yoon M., Jee M. J., 2021, *Astrophys. J.*, 908, 13

van Daalen M. P., Schaye J., Booth C. M., Vecchia C. D., 2011, *Mon. Not. Roy. Astron. Soc.*, 415, 3649

van Daalen M. P., McCarthy I. G., Schaye J., 2020, *Mon. Not. Roy. Astron. Soc.*, 491, 2424

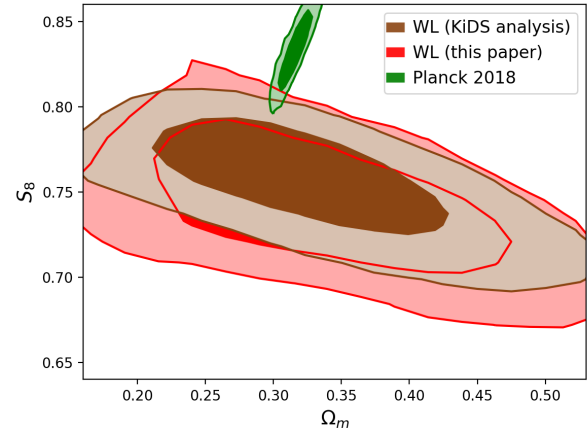


Figure A1. Comparison of the posterior distribution from our analysis (red) and the KiDS results (brown). The contours from Planck are shown in green for reference. The details about the difference between the two analysis pipelines are given in the text.

APPENDIX A: COMPARISON WITH THE ORIGINAL KiDS ANALYSIS

Throughout this paper, we use the weak-lensing band power data vector and covariance matrix provided by the KiDS-1000 science team (Asgari et al. 2021). However, our analysis pipeline differs from the one used in the original KiDS analysis (see discussion in Sec. 3). Most notably, in order to predict the matter power spectrum, we rely on the revised halofit method (Takahashi et al. 2012) instead of the HMcode (Mead et al. 2015). Furthermore, our initial transfer function is obtained using the Eisenstein & Hu (1998) fitting function (instead of the Boltzmann solver Class) and we neglect any effects from massive neutrinos.

Next to the differences in the prediction pipeline, we do not vary the same parameters during our MCMC sampling runs. Most notably, we use the baryonification model with seven free baryonic parameters as opposed to one parameter used by the KiDS team. On the other hand, we abstain from varying any parameters related to the redshift distribution of the source galaxies.

In Fig. A1 we compare the $S_8 - \Omega_m$ posteriors from this paper (red) with the ones obtained by the KiDS team (brown). Our contours are somewhat broader, extending further towards small values of S_8 . We speculate this to be an effect of the increased number of baryonic parameters, which also allows for scenarios featuring a baryonic boost (instead of a suppression) of the power spectrum. Compared to the posterior from KiDS, our contours are also slightly shifted downwards. This effect is most visible when focusing on the 68 percent confidence region. This shift could be a consequence of using the revised halofit model instead of HMcode. Indeed, it has been shown using KiDS 450 data that moving from HMcode to halofit may lead to a bias on S_8 of up to 0.3 standard deviations (Joachimi et al. 2021).

APPENDIX B: BARYONIC PARAMETER CONSTRAINTS FROM SPECIFIC DATA COMBINATIONS

In Sec. 4 we show the posterior contours of the seven baryonic parameters using data from the KiDS-1000 WL band power data

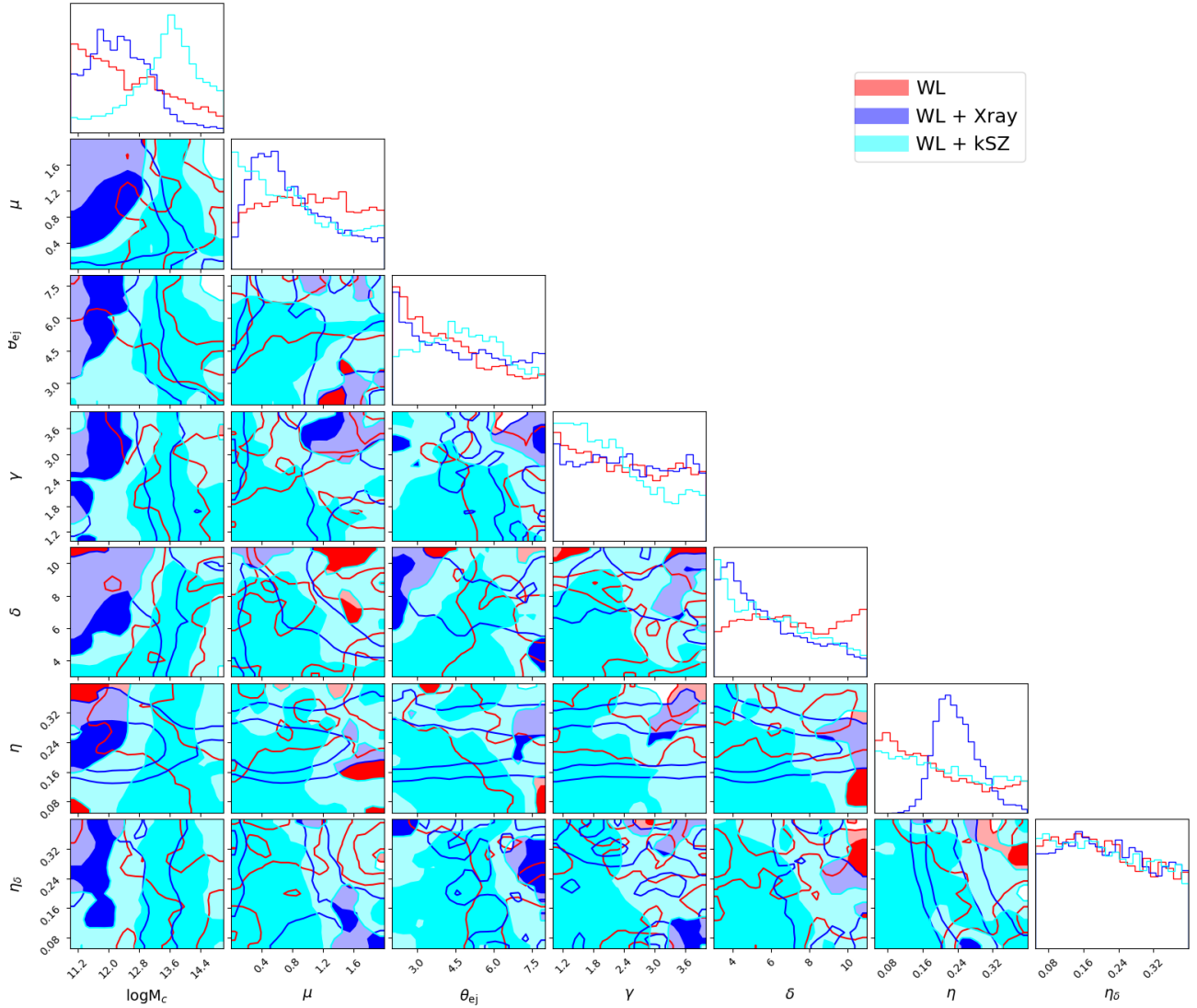


Figure B1. Posterior contours of the baryonification model parameters at 68 and 95 percent confidence level. Results based on KiDS-1000 weak-lensing data alone are shown in red. Results from the combined WL + Xray and WL + kSZ data sets are shown in blue and cyan, respectively. Posterior contours from the full WL + Xray + kSZ data combination are illustrated in Fig. 4 of the main text.

alone and from the combined WL + Xray + kSZ data vector. In this appendix we also discuss the intermediate cases, namely the WL + Xray and the WL + kSZ data combinations. This allows us to investigate more subtle differences between the results from the X-ray gas (and stellar) fractions, on the one hand, and the stacked kSZ profiles, on the other hand.

Fig. B1 shows the posterior contours of the baryonification parameters for the WL only (red), the WL + Xray (blue), and the WL + kSZ (cyan) data sets. The first has already been shown in Fig. 4 and is added here as a reference. There are several notable differences between the blue and the cyan posteriors. Most importantly, the M_c -parameter, describing the mass-dependence of the gas profile, is centred around $\sim 10^{12} M_\odot/h$ in the WL + Xray and around $\sim 4 \times 10^{13} M_\odot/h$ in the WL + kSZ case. This indicates that the observations based on the kSZ effect favour a stronger feedback regime compared to the X-ray data. It is therefore not surprising that the Σ_8 posterior distribution of the former is slightly shifted towards the results from Planck (see Fig. 6).

Another slight difference can be observed in the behaviour of μ , the parameter describing how strongly low-mass and high-mass haloes differ in their gas profile. While in the WL + Xray case, very small values of μ are disfavoured, they remain valid in the WL + kSZ scenario. This difference can be explained by the fact that the kSZ profiles are limited to a halo mass of $\sim 10^{13} M_\odot/h$. The X-ray gas fractions, on the other hand, probe halo mass scales 10^{13} and $10^{15} M_\odot/h$ allowing them to rule out values of μ , where there is little or no evolution of the gas profiles with halo mass.

Finally, there is a visible difference between the blue and cyan contours of the stellar parameter η , which is well constrained in the WL + X-ray and completely unconstrained in the WL + kSZ case. This is a direct consequence of the stellar fractions that are part of the X-ray data set. All other parameters shown in Fig. B1 behave similarly in both cases.

This paper has been typeset from a \LaTeX file prepared by the author.